Journal of Marine Science and Application (2025) 24: 1174-1193
https://doi.org/10.1007/s11804-025-00645-0

RESEARCH ARTICLE

Impact of Water Depth on the Resistance of a Mini-Bulk Carrier: An Experimental and Numerical Study

T. Jebin Samuvel[1] **and R. Vijayakumar**[1]

Received: 23 August 2024 / Accepted: 11 November 2024

Abstract

Water depth significantly affects ship resistance, which, in turn, influences fuel consumption. Furthermore, the urgent need to reduce carbon emissions for environmental sustainability highlights the importance of applying drag reduction methods to shallow-water vehicles. To effectively employ these methods, the initial step entails an in-depth investigation of how shallow water impacts the resistance and flow dynamics of a mini-bulk carrier. This study extensively analyzes the hydrodynamic characteristics of mini-bulk carriers, focusing on the impact of shallow water on resistance and flow dynamics utilizing a combination of experimental tests and numerical analyses. This study emphasizes the interaction between the hull and the shallow seabed. This study also highlights increased frictional drag and significant residual resistance by analyzing the total resistance at various speeds in shallow waters. The results of five key factors influencing resistance in shallow waters, namely, boundary layer thickness, shear stress, velocity and pressure, turbulence, and waves, are discussed. A decrease in water depth accelerates the flow under the hull, increasing shear stress and resistance. The accelerated flow reduces the gap between the hull and the shallow seabed, elevating water pressure and increasing sinkage and resistance. Heightened turbulence in shallow water intensifies Reynolds stress, augmenting friction and viscous resistance.

Keywords Shallow water; Mini bulk carriers; Resistance; Computational fluid dynamics; Ship hydrodynamics

1 Introduction

Ship resistance directly impacts fuel consumption and emissions during maritime transportation. Increased resistance leads to higher fuel consumption, resulting in significant emissions of pollutants and greenhouse gases. Therefore, minimizing ship resistance is crucial for reducing fuel consumption and emissions. Various methodologies for mitigating drag on maritime vessels exist, all aimed at identifying effective methods to reduce the overall resistance and enhance the hydrodynamic efficiency of the ship. Pressure drag can be reduced by modifying the shape of the vessel using advanced hull designs or optimization techniques or by installing energy-efficient devices, such as flaps and hull vanes (Hemanth Kumar and Vijayakumar, 2020a, 2020b; Soma and Vijayakumar, 2023a, 2023b; Tripathi and Vijayakumar, 2024). Furthermore, considering the viscous component of overall drag, specifically frictional drag, is paramount. Frictional resistance contributes approximately 80% of the total resistance of ships with a lower Froude number, making it the primary target for reduction efforts (Sindagi and Vijayakumar, 2020). Different techniques such as implementing riblets, surface heating, using polymer additives, creating surface vibration, and applying air lubrication help mitigate frictional drag.

Notably, most of these methods, except for air lubrication, are not environmentally friendly or economically viable and often require extensive maintenance. Air lubrication systems (ALS) mitigate frictional drag by introducing gas to the vicinity of the liquid flow near the wall. Previous research has shown that this method significantly reduces the frictional resistance between the hull surface and the water by up to 80% under optimal conditions (Sindagi et al., 2021, 2020a, 2020b; Sindagi and Saxena, 2016; Jebin Samuvel et al., 2022).

Article Highlights

- The overall resistance of a mini-bulk carrier ship was examined at various velocities for 3 different shallow depths.
- The study focused on how boundary layer thickness, shear stress, velocity and pressure, turbulence, and waves affect the shallow water resistance.
- Pressure gradients can detach and reconnect flow, creating turbulent eddies and vortices that increase ship turbulence and resistance.
- These changes inside the boundary layer significantly impact Reynolds stress, increasing the resistance.

✉ T. Jebin Samuvel
samuveltjs@gmail.com

[1] Department of Ocean Engineering, Indian Institute of Technology Madras, Chennai 600036, India

Research indicates that air lubrication methods are particularly suitable for inland water vessels, as highlighted by Gorbachev and Amromin (2012), Jebin Samuvel et al. (2022). The literature proposes that ALS can effectively reduce the frictional drag of ships navigating narrow channels or shallow waters, thus promoting the adoption of the ALS method for shallow-water mini-bulk carriers. However, optimizing performance for improved resistance and power efficiency in shallow waters is essential to comply with the Energy Efficiency Existing Ship Index standards for mini-bulk carriers of established dimensions. Therefore, before implementing drag reduction techniques on mini-bulk carriers intended for shallow water environments, the impact of shallow water on resistance properties and flow field dynamics needs to be understood. This understanding is crucial because applying these techniques to vessels designed for shallow depths poses additional challenges. Accurately assessing ship resistance in shallow or restricted water scenarios is vital for reducing resistance and determining the minimum power requirements.

As ships transition from deep to shallow waters, the pressure surrounding the hull changes because of variations in water depth, causing an increase in flow velocity around the hull. In addition, this transition creates a scenario where the tangential velocity reaches zero, resulting in an additional boundary layer at the bottom. In contrast to deep water conditions, the higher speed and the presence of an additional boundary layer result in a thinner boundary layer surrounding the hull. This thinner boundary layer leads to a more pronounced velocity gradient, elevating the surface shear stress of the ship. Consequently, this heightened shear stress level amplifies ship resistance, adversely affecting its speed–power characteristics and overall operational efficiency. Therefore, the accurate prediction of resistance under shallow water conditions is crucial.

The behavior of ships under shallow water conditions has been extensively investigated in ship theory, drawing significant interest from marine engineers who have devoted considerable time and effort to its study. Initially, prediction approaches focused on addressing speed loss in shallow water, as outlined by Schlichting (1934). However, this method only applies to subcritical Froude numbers. In a subsequent study conducted by Lackenby (1964), Schlichting's approach was refined through modifications to the speed correction method, expanding its range of applicability. A correlation between the mean effective speed and the effective hydraulic obstruction was detected in the research conducted by Jiang (2001). The mean sinkage affects this connection, whereas the water depth has a negligible effect. The effectiveness of these methods relies on the accuracy of predictions in deep water and is based on reducing drag experienced under such conditions. As mentioned, prediction methods have shown practical efficacy but are often limited to depth, Froude number, and hull shape. By contrast, model tests provide a more practical approach to investigating shallow water phenomena. The study presented various representations obtained from extensive model tests to demonstrate the contrasting ship resistance in shallow and deep sea environments. Studies conducted by Elsherbiny et al. (2020), Lataire et al. (2012), Mucha (2017), Zeng et al. (2017), Raven (2019, 2018), Xu et al. (2017), Zeng et al. (2018) focused on resistance, squat, ship maneuvering, and propulsion and provided significant reference data for the successful design and operation of modern shallow and inland waterway vessels.

Computational fluid dynamics (CFD) has emerged as a viable option for analyzing ship characteristics in shallow water, as highlighted by Tabaczek (2008) Tezdogan et al. (2016), Zeng et al. (2019b). Terziev et al. (2018) conducted an extensive investigation to assess the effectiveness of numerical methodologies in accurately depicting the hydrodynamic characteristics of ships navigating in shallow water environments. In contrast to traditional model tests, CFD provides a comprehensive understanding of the fundamental fluid dynamics principles, enabling a more precise calculation of the forces applied to the surface of the ship. Ship resistance analysis in shallow water primarily employs numerical simulations and ship model tests. In their study, Mucha et al. (2018) conducted model tests at three distinct depths to investigate the impact of depth and separation distance on resistance and propulsion. Their findings indicated that hydrodynamic interactions and flow restrictions influenced the resistance and propulsion characteristics. The observed sensitivity to variations in water depth and distance to the wall exhibited a consistent pattern following the underlying theoretical framework. The wave resistance shows a decreasing trend as the velocity reduces, whereas viscous pressure is the primary factor influencing resistance at lower velocities. In their study, Zeng et al. (2019a) proposed a revised International Towing Tank Conference (ITTC) 57 correlation line explicitly tailored for shallow water conditions. As channel depth decreases, total frictional resistance increases, which is further exacerbated by sinkage and trim effects, resulting in deviations from the ITTC 57 recommendations. Hull frictional resistance increases until the water depth to draft (H/T) ratio reaches 1.2. At $H/T < 1.2$, the frictional resistance coefficient is equal to that under deep water conditions. The primary factor impacting frictional resistance in extremely shallow water is the hull shape (ship fullness). Different ships have different shear stress distributions on the hulls. For higher C_b, a negative gradient of shear stress was detected at the flat bottom of the ship in the longitudinal direction, which results in lower C_f in extremely shallow water. Su et al. (2023) proposed that the impact of water depth on frictional resistance is relatively insignificant, whereas the residual resistance increases with a decrease in water depth. High pressure at the bow and stern, along

with low pressure in the middle of the bottom, can result in sinkage and trim, which can adversely affect the safe maneuvering of the vessel and cause increased resistance when operating in shallow water. Chen et al. (2021) noted that changes in water depth affect the pressure distribution around the vessel, resulting in increased hydrodynamic forces and resistance and reduced maneuverability.

According to Tang et al. (2020), accurately estimating viscous resistance in shallow water is crucial for vessels operating at low Froude numbers. As the ratio between water depth and ship draft decreases, the shallow water effect intensifies, increasing resistance and reducing maneuverability. Rotteveel and Hekkenberg (2015) stated that the impact of shallow water on resistance becomes significant when the ratio of water depth to ship draft (H/T) is < 2. Pressure and frictional resistance increase proportionally with the H/T ratio. For shallower water with H/T ratios of 1.66 and 1.2, the pressure resistance increase exceeds the frictional resistance increase. The shallow water effect significantly impacts the resistance experienced by the bow and stern of a vessel. According to Raven (2012), a significant correlation between the decreasing water depth in shallow water and a substantial increase in viscous resistance exists. This increase in viscous resistance was comparable between model ships and full-scale ships, especially in shallow scenarios. The observed increase in resistance in shallow water primarily stems from viscous resistance rather than an increase in wave or residual resistance. The decrease in this aspect is observed from the model scale to the ship scale, leading to reduced resistance predictions at full scale in shallow water. In their study, Song et al. (2023) investigated the influence of surface roughness on ship resistance and squat in shallow waters. According to their results, when the H/T ratio = 1.1 and F_h = 0.44, pressure resistance accounted for approximately 47.8% of the total resistance for a smooth hull and 51.4% of the total resistance for a rough hull.

In the study conducted by Ji et al. (2012), simulations were employed to analyze the wave patterns generated by convoys navigating through narrow waterways. They investigated the relationship between geometric and kinematic variables, such as ship dimensions and velocity, and the resulting wave characteristics produced by the vessels. In addition, their primary objective was to predict the extent of water surface deformation caused by the passage of these vessels. A significant pressure gradient close to the hull of the ship has the potential to influence the wave generation process. Terziev et al. (2021) examined the impact of shallow and restricted water conditions, particularly in cases with limited space between the hull of a ship and the canal or seabed. The importance of these effects lies in the pivotal role of viscosity in such scenarios. In their study, Li et al. (2023) investigated the phenomenon of unsteady wash waves generated when a ship encounters variations in water depth. The dynamic force produced by the movement of the ship interacts with the changes in water depth, revealing the occurrence of upstream waves and the associated oscillatory wave resistance. The formation of an upstream leading wave elevation significantly increases the vertical force exerted on the ship. The fluid flow velocity in the forward direction significantly impacts the height of the leading wave. Specifically, the elevation of the upstream wave increases according to a power function of Fr_h^n, where the exponent n falls within the range of 3 to 4.

The study conducted by (Tuck, 1978) extensively explored the hydrodynamic challenges that vessels encounter when navigating confined water passages. Their research delved into the fundamental physical phenomena occurring during the interactions between ships and the constraints imposed by surrounding flow conditions. Kumar and Anantha Subramanian (2007) investigated the impact of tank walls on the resistance of ship models during model tests. Their research revealed conclusive evidence of a significant effect on residual resistance. Their findings are consistent with numerical predictions and values obtained from Geosim tank tests. Vantorre et al. (2002) conducted a comprehensive investigation into the hydrodynamic interactions between ships and banks, specifically focusing on the impact of bank geometry.

Numerical simulations and ship model tests are the primary approaches for investigating ship resistance in shallow water. However, further research is necessary to understand the resistance characteristics of shallow-water mini-bulk carrier vessels. Mini-bulk carriers are specifically designed to operate in shallow waters, providing access to ports and terminals with limited draft. This feature enhances connectivity and commercial opportunities by allowing them to serve areas inaccessible to larger vessels. Continued research and development are essential to improve their effectiveness in reducing resistance and fuel consumption. To achieve environmental sustainability, carbon emissions need to be reduced. Thus, drag reduction techniques for shallow-water vehicles need to be implemented. To do this effectively, examining how shallow water affects the resistance and flow dynamics of mini-bulk carriers is essential. This investigation is the first step toward successfully applying drag reduction methods. This study primarily focuses on numerical methodologies for analyzing the resistance characteristics of vessels in shallow water environments. Mini-bulk carriers with low Froude numbers in shallow water have not been extensively investigated. Therefore, this study examines the effect of external conditions on the performance of a mini-bulk carrier, including resistance, wave generation, pressure distribution, and flow field. This study also examines the correlation between the water depth and the resistance of mini-bulk carrier ships, analyzes the various factors contributing to the shallow water effect, and determines the best practices for investi-

gating the influence of shallow water on resistance. Numerical studies were conducted on a 1 : 23 ratio model scale mini-bulk carrier under various water depth conditions. The objective was to analyze the resistance performance of the ship model under shallow water conditions and identify potential areas for drag reduction using Air Lubrication Drag Reduction methods. The remainder of this paper provides a comprehensive explanation of the experimental techniques used, an overview of the numerical method employed, a discussion of the uncertainties associated with the numerical techniques used, a presentation and analysis of the results obtained, a thoughtful discussion of the findings, and a succinct conclusion summarizing the key findings and proposing potential avenues for future research.

2 Experimental method

The model tests were conducted in accordance with the ITTC (2011) prediction method and followed the recommendations outlined in QSG of the 28th ITTC (2021). The experiments were conducted at the towing tank facility of the Indian Institute of Technology Madras.

The vessel under investigation is a mini-bulk carrier, specifically a twin-screw river–sea vessel designed for transporting bulk cargo. Table 1 provides the main particulars and Figure 1 shows the body plan and 3D computer-aided design model of the mini-bulk carrier. The vessel was fabricated using reinforced fiberglass, and a geometric scale ratio of 1 : 23 was applied. The hull design includes twin aft skegs to meet the maneuvering requirements within the confined operational area. With $Fr = 0.152$, this vessel is categorized as a slow-speed ship. A 3-mm-diameter trip wire was attached to the hull at 5% aft of the forward perpendicular to simulate turbulence. The distribution of ballast weight was made to replicate the longitudinal center of gravity (LCG) position observed in the prototype. The scale of the model was determined by considering hydrodynamic factors, such as the dimensions of the vessel, Froude number, and limitations of the towing tank. To measure the drag forces exerted on the model, a load cell with a maximum capacity of 50 kg was strategically placed at the tow point of the vessel, precisely at the LCG. In addition, a motion reference unit continuously monitored the trim angles of the model throughout the study. Furthermore, numerical analysis was conducted using this scaled model. Figure 2 depicts the physical model with skeg and trip wire.

2.1 Shallow-water towing tank

The towing tank dimensions are 82 m in length, 3.2 m in width, and 2.8 m in depth. The towing tank carriage has a maximum attainable velocity of 4 m/s and is equipped

Table 1 Main particulars

Main particulars	Prototype	Model
Scale	1	23
Length overall (m)	122.25	5.25
Beam, B (m)	20	0.87
Depth (m)	7.2	0.31
Design draft, T (m)	4.8	0.209
Longitudinal center of gravity (m)	(61.64, 0, 4.807)	(2.68, 0, 0.209)
Mass displacement (tonnes)	102.32	0.812
Maximum speed (m/s)	5.144	1.073
Froude number, Fr	0.045 4 to 0.151	

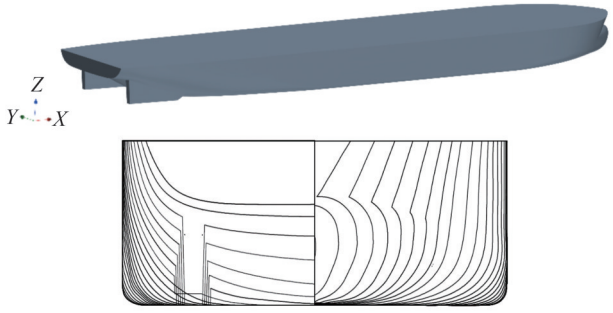

Figure 1 Body plan and 3D computer-aided design model of a mini-bulk carrier

Figure 2 Model of the mini-bulk carrier

with a precise speed control system provided by Rockwell Automation Systems. The river–sea model was secured to the towing carriage using two pivot levers and a brake pad. Specific constraints were applied to the model to mitigate the impact of surge, sway, yaw, and roll motions, thereby enabling the model to have pitch and heave motions. The existing towing tank facility has a depth of 2.8 m, which limits experimentation to shallow water conditions. A detachable, reusable, and depth-adjustable false bottom was made and utilized to replicate the shallow water conditions for shallow water experiments, as shown in Figure 3. This false bottom was designed to ensure that it did not interfere with the regular operations of the towing tank and comprised 48 platforms, each measuring 1.5 m long (along the length of the towing tank) and 3.2 m wide. Proper sealing and waterproofing of the false bottom interface with the basin walls are crucial for preventing water loss, avoiding leakage, maintaining the integrity of the experimental setup, and ensuring measurement accuracy. The structural integ-

rity and stability of the false bottom must be ensured to withstand the hydraulic forces exerted by flowing water, wave action, or other experimental conditions. Proper design, materials selection, and structural reinforcement are essential to prevent the deformation, failure, or collapse of the false bottom during experimentation. Stiffeners were added to the false bottom to prevent bending. Proper care is taken throughout the experiment to ensure proper installation and that the current false bottom setup works.

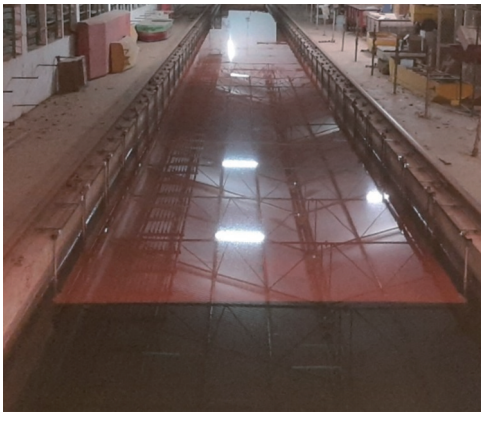

Figure 3 Shallow water towing tank

2.2 Test conditions

To comprehensively explain the impact of shallow water on ship resistance, parameters, such as H/T or L/H, along with the depth Froude number (Fr_h), are typically employed. According to the ITTC, the shallow water effect becomes notable when the ratio of channel height to draft is <4. In this study, tests were conducted with H/T (as shown in Figure 4) and Froude number. Blockage correction was employed during the trial to rectify the experimental outcome, which was affected by the interference resulting from the dimensions of the hull model and the towing tank. The Schuoneter equation can be used to calculate the blockage correction values (ITTC, 2021):

$$\frac{\Delta V}{V} = \frac{m}{1 - m - Fr_h^2} + \left(1 - \frac{R_V}{R_T}\right) \times \frac{2}{3} Fr_h^{10} \tag{1}$$

where

$$m = \frac{A_x}{A} \tag{2}$$

2.3 Test matrix

The experimental model tests were conducted at four distinct water depths, characterized by H/T ratios of 1.5 and 1.7 (representing extremely shallow water), H/T ratio of 2 (representing shallow water), and H/T ratio of 24 (representing deep water). These tests covered a range of speeds

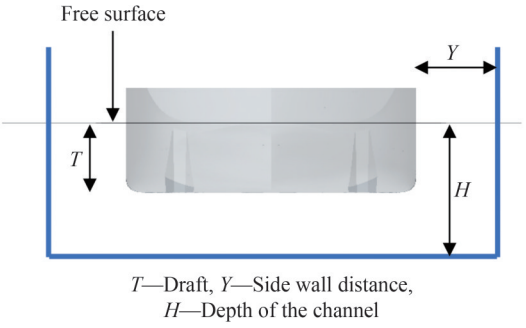

T—Draft, *Y*—Side wall distance,
H—Depth of the channel

Figure 4 Schematic diagram of shallow water

from 0.429 m/s to 1.73 m/s, corresponding to vessel speeds between 4 kn and 10 kn. The corresponding Froude numbers ranged from 0.060 to 0.151. The test conditions are outlined in detail in Table 2.

Table 2 Test conditions

Model speed	Fr	Fr_h		
	Deep $H/T = 24$	Shallow $H = 2T$	Shallow $H = 1.7T$	Extremely shallow $H = 1.5T$
0.429	0.060	0.211 9	0.230	0.245
0.536	0.075	0.264 8	0.287	0.306
0.644	0.090	0.317 8	0.345	0.367
0.751	0.105	0.370 8	0.402	0.428
0.858	0.121	0.423 7	0.460	0.489
0.965	0.136	0.476 7	0.517	0.550
1.073	0.151	0.529 7	0.575	0.612

3 Numerical method

The application of Reynolds-averaged Navier–Stokes (RANS) methods is a rapidly progressing area in ship hydrodynamics. Through computational simulations, the primary objective is to analyze dynamic variations in ship behavior, including trim, sinkage, surface pressure, and hydrodynamic forces. The fundamental fluid flow equations are the continuity and Navier–Stokes equations. The use of CFD techniques, such as the finite volume method, enables the simulation of intricate fluid flow scenarios without further simplification ("Best practices for ship resistance test simulations in shallow water", 2019).

3.1 Governing equations

The following are the governing equations for the incompressible turbulence flow that satisfy the conservation of mass and momentum:

$$\frac{\partial \rho}{\partial t} + \nabla \cdot \left(\rho \bar{\boldsymbol{u}}\right) = 0 \tag{3}$$

$$\frac{\partial \left(\rho \bar{\boldsymbol{u}}\right)}{\partial t} + \nabla \cdot \left(\rho \bar{\boldsymbol{u}} \otimes \bar{\boldsymbol{u}}\right) = -\nabla \cdot \bar{P}\boldsymbol{I} + \nabla \cdot \boldsymbol{T} + f_b \tag{4}$$

where $u = (u_1, u_2, u_3)$; $\bar{\boldsymbol{u}}$ is the mean velocity vector, which denotes the velocity component along the x, y, and z axes, respectively; $\bar{P}\boldsymbol{I}$ is the mean pressure; ρ is the density of the fluid; μ is the dynamic viscosity; $\boldsymbol{T}$ is the Reynolds stress tensor, which can be solved using a turbulence model or transport equation; and $\boldsymbol{I}$ is the identity tensor.

The Reynolds stresses in the eddy viscosity models are assumed to be related to the mean velocity gradients, turbulent kinetic energy (TKE), and eddy viscosity.

$$\boldsymbol{T} = \mu_t \left[\nabla \bar{\boldsymbol{u}} + \left(\nabla \bar{\boldsymbol{u}}\right)^{\mathrm{T}}\right] - \frac{2}{3}\rho k \boldsymbol{I} \tag{5}$$

where μ_t is the eddy viscosity, and k is the TKE, which can be solved using turbulence models such as $k-\varepsilon$ and $k-\omega$.

The solver incorporates the volume of fluid (VOF) method to accurately model the interaction between the free surface and the fluid in this simulation, thereby accounting for the effects of the free surface. A supplementary transport equation is solved to forecast the dispersion and motion of air and water. The scalar volume fraction quantifies the proportion of space occupied by a particular phase and indicates the location of the boundary between phases for each control volume in the fluid domain. The high-resolution interface-capturing scheme, introduced by Muzaferija and Peric (2017), ensures interface sharpness. The pressure and velocity are solved independently using the SIMPLE algorithm and a second-order time discretization method.

3.2 Domain and boundary conditions

The computational domain is arranged according to the guidelines provided by ITTC (2021). The inlet is located more than one ship length ahead of the front perpendicular (FP) and induces flow in the opposite direction of the x-axis under a velocity inlet boundary condition. Determining the breadth and downstream expansion of the area is critical when dealing with shallow water circumstances. The Kelvin wave pattern can change considerably when nonlinear wave production and propagation processes occur in certain circumstances.

The outlet is positioned downstream of the aft perpendicular (AP) at a distance equal to three times the length of a ship and functions as a pressure outlet, maintaining constant hydrostatic pressure and preventing reverse flow. Table 3 delineates the selected boundary conditions for both shallow and deep water scenarios. The side wall is situated at a distance of 1.3 ship lengths away to minimize interface effects, as per Table 4 for selecting the side wall interface "Best practices for ship resistance test simulations in shallow water" (2019), ITTC (2011). Both the side and lower boundaries are designated as moving no-slip walls. The laboratory coordinate system is located at the stern keel, with the positive x-direction toward the bow, the positive y-direction toward the beam (port side), and the positive z-direction toward the waterline. The flow is simulated toward the negative x-direction. To expedite the solution process, wave damping has been applied perpendicular to the boundaries at the exit, spanning a distance that exceeds 1.3 times the length of the ship. The upper limit of the domain, identified as a velocity inlet, is positioned approximately one ship length above the undisturbed waterline. The chosen method for determining the bottom and side boundaries involves assigning a relative velocity equivalent in magnitude but opposite in direction to the speed of the ship. This condition ensures the occurrence of relative motion between the seabed and the side when the flow is introduced to the domain. Consequently, from the perspective of the ship, the flow, bottom, and side all move downstream at the same speed. Figure 5 provides a graphical representation of the computational domain.

Table 3 Boundary conditions

Sl. No.	Boundary	Deep water	Shallow water
1	Inlet and top	Velocity inlet	Velocity inlet
2	Outlet	Pressure outlet	Pressure outlet
3	Sidewall and bottom	Velocity inlet	Moving no-slip wall

Table 4 Side wall distance

Depth	Distance	Experiment in N	Numerical simulation in N	Difference in percentage
$1.7T$	$1Y$	15.230	14.691	3.35
	$1.3Y$		14.718	3.30

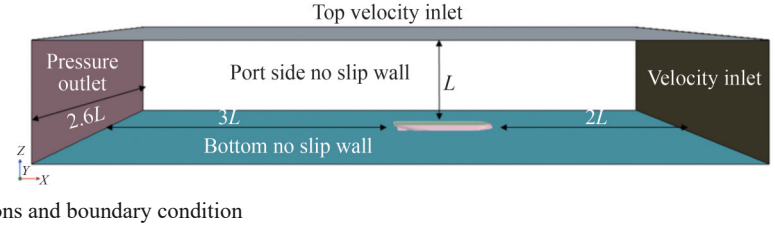

Figure 5 Domain dimensions and boundary condition

3.3 Mesh

The computational domain is divided into trimmed hexahedral control volumes, employing a finite volume approach. These control volumes predominantly consist of hexahedral cells, with strategically placed trimmed hexahedral cells near surfaces to represent curvature accurately. The background mesh covers the entire numerical domain and comprises hexahedral cells, with refinement regions surrounding the free surface and the hull, as depicted in Figure 6. Mesh refinement is applied to the free surface and the Kelvin wave pattern, as illustrated in Figure 7. The mesh gradually transitions to a coarser resolution as it moves away from the model. Consequently, the domain was discretized into 10 million cells to simulate shallow water conditions and 8 million cells to simulate deep water conditions. The fluid dynamics within the under-keel clearance (UKC) zone need to be carefully considered when engaging in activities in shallow water, mainly when the boundary layer thickness of the ship is comparable to the distance separating it from the seabed. The downstream region often exhibits discernible flow characteristics, such as notable separation, anisotropic turbulent momentum transport, and secondary recirculation. Refinement within the UKC zone, mainly on the lower wall, is advisable.

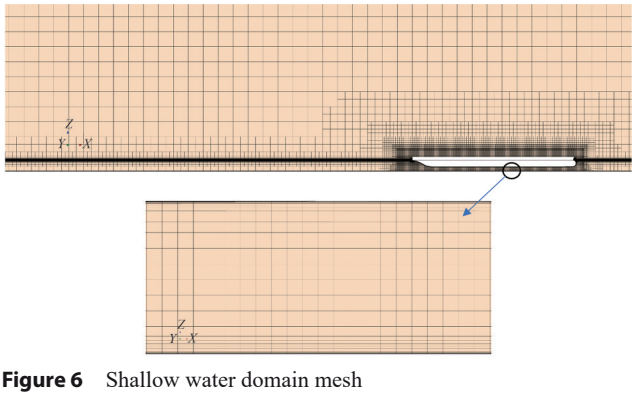

Figure 6 Shallow water domain mesh

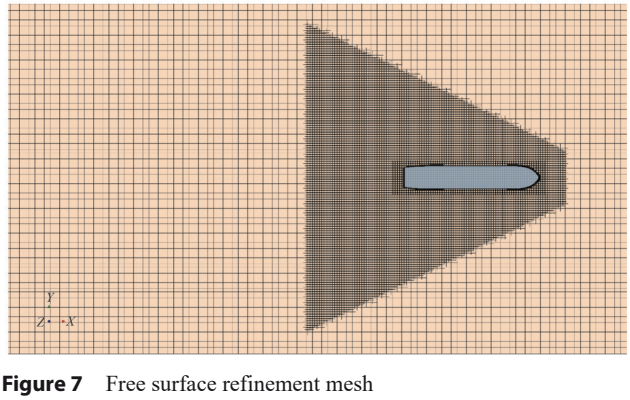

Figure 7 Free surface refinement mesh

The overset methodology was employed to generate numerical grids, as shown in Figure 8. The overset mesh was strategically positioned close to the hull, allowing it to move in sync with the hull during simulations, particularly regarding the sinkage and trim of the ship model. The interpolation occurs within the overlap region, providing a more significant data transfer area than the nonoverlapping hybrid mesh. Thus, employing an overset mesh configuration could potentially enhance computational efficiency compared with a nonoverlapping hybrid mesh, assuming similar levels of accuracy. The independent construction of an overset mesh for each component within the domain without considering grid alignment for each component has been proposed as a viable approach. This approach enables the manipulation of the rotation and displacement of the mesh to adjust the trim and sinkage effects on the ship.

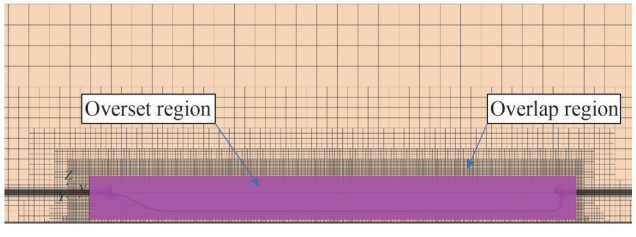

Figure 8 Overset mesh

Similarly, the adjustment of water depth can be conveniently achieved by altering the underlying mesh structure. To accurately represent the movement of the boundary layer near the surface of the vessel, prism layers are created near the hull surfaces. The determination of the cell dimensions in the prism layer mesh depends on the wall y^+ criterion, which is related to the turbulence model utilized in the simulations. In all cases, a wall function is employed to maintain a y^+ value of < 1. The chosen methodology utilizes a highly intricate mesh near the model and on the unconstrained surface to accurately capture any variations in fluid dynamics. Figure 9 illustrates that the wall y^+ criterion was maintained at the underwater part of the hull with $H/T = 1.7T$ for $Fr = 0.151$.

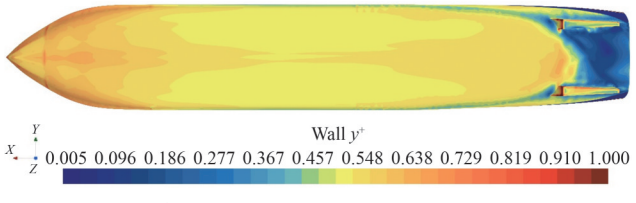

Figure 9 Wall y^+ criterion

3.4 Solver settings

The efficacy of two-equation eddy viscosity models has been demonstrated in yielding satisfactory results when applied under shallow water conditions and realistic forward velocities. A computational model, combining the VOF method for multiphase flow and a gravity model, calculates the pressure and resultant forces generated by

wave formation. However, the selection and activation of higher-order constitutive relations and application of curvature correction in the STAR-CCM+ software when dealing with shallow water is advisable. The inclusion of curvature correction is crucial for enhancing the accuracy of the analysis of the anisotropic transmission of turbulent momentum and recirculation, significantly impacting resistance calculations. Alternative configurations under flow conditions provide a more precise assessment of resistance increase in shallow water than conventional configurations ("Best practices for ship resistance test simulations in shallow water", 2019). The use of the two-phase VOF model enables the resolution of a singular set of equations concerning the preservation of mass, momentum, and energy, accurately representing the corresponding fluid phases. This methodology assumes that all phases, whether air or water, exhibit identical characteristics in their flow field when considered within a control volume, making the imposition of a boundary condition at the interface unnecessary. The model utilizes pertinent features and volume fractions of elemental phases to calculate fluid properties, including density and viscosity. Table 5 lists the solver settings employed under shallow water conditions.

Table 5 Solver settings

Parameter	Settings
Solver	3D, unsteady, implicit
Turbulence model	SST $k-\omega$
Wall treatment	All wall y^+ treatment
Multiphase model	Volume of fluid (VOF)
Time	First-order upwind
Pressure discretization	Standard
Pressure velocity coupling	SIMPLE
Compressibility and curvature correction option	Enabled

4 Uncertainty in numerical methods

4.1 Grid vonvergence index

A previous study evaluated grid independence to address the discretization error in the solution. An investigation into grid convergence was conducted by Richardson (1910) to assess the uncertainty error in CFD studies. However, the assessment remains unaffected by the results derived from CFD. Celik et al. (2008) presented a comprehensive approach to determining discretization uncertainty in CFD applications, which involved implementing a two-grid study to examine two different water depths, i.e., deep water conditions with H/T of 24 and 1.7. Fr is set as 0.105, and the refinement ratio is determined to be the square root of 2. Following the guidelines outlined by the ITTC, a time step of 0.01 s is used.

In estimating uncertainties, three meshes, namely, a fine mesh grid denoted as N1, a medium mesh grid denoted as N2, and a coarse mesh grid denoted as N3, are employed. The fine mesh grids contain 29.3×10^6 cells, the medium mesh grids contain 10.04×10^6 cells, and the coarse mesh grids contain 3.67×10^6 cells. The parameter selected for the convergence study was the resistance of the vessel. The following steps are used to analyze grid independence. Table 6 shows the uncertainty under deep and shallow water conditions.

Table 6 Mesh grid independence

Depth	Deep $H/T = 24$			Shallow $H/T = 1.7$		
Factors	Fine mesh grid (1)	Medium mesh grid (2)	Coarse mesh grid (3)	Fine mesh grid (1)	Medium mesh grid (2)	Coarse mesh grid (3)
Number of cells (N) $\times 10^6$	23.5	8.14	2.87	29.345 8	10.387 7	3.674 3
Absolute value of resistance (φ)	10.242 3	10.364 0	10.876	14.642 3	14.718 0	14.976 0
Grid refinement factor (r_{21}, r_{32})		$r_{21} = 1.424$ $r_{32} = 1.415$			$r_{21} = 1.414$ $r_{32} = 1.415$	
Absolute difference (ε_{21}, ε_{32})		$\varepsilon_{21} = 0.121\ 7$ $\varepsilon_{32} = 0.512\ 0$			$\varepsilon_{21} = 0.076\ 3$ $\varepsilon_{32} = 0.257\ 4$	
Apparent order (p)		$p = 4.067\ 5$			$p = 3.512\ 5$	
Extrapolated values (ϕ_{ext}^{21}, ϕ_{ext}^{32})		$\phi_{\text{ext}}^{21} = 10.204\ 4$ $\phi_{\text{ext}}^{32} = 10.199\ 3$			$\phi_{\text{ext}}^{21} = 14.610\ 2$ $\phi_{\text{ext}}^{32} = 14.610\ 6$	
Approximate relative error (%) (e_a^{21}, e_a^{32})		$e_a^{21} = 1.19$ $e_a^{32} = 4.94$			$e_a^{21} = 0.52$ $e_a^{32} = 1.75$	
Extrapolated relative error (%) (e_{ext}^{21}, e_{ext}^{32})		$e_{\text{ext}}^{21} = 1.56$ $e_{\text{ext}}^{32} = 1.62$			$e_{\text{ext}}^{21} = 0.74$ $e_{\text{ext}}^{32} = 0.74$	
GCI (%)		$\text{GCI}^{21} = 0.46$ $\text{GCI}^{32} = 1.99$			$\text{GCI}^{21} = 0.27$ $\text{GCI}^{32} = 0.92$	

The average size of the grid:

$$h = \left(\frac{1}{N} \sum_{i=1}^{N} \left(\Delta V_i \right) \right)^{1/3} \tag{6}$$

where ΔV_i is the volume of the ith cell.

Apparent order (p):

$$p = \frac{1}{\ln\left(r_{21}\right)} \left| \ln \left| \frac{\varepsilon_{32}}{\varepsilon_{21}} \right| + q(p) \right| \tag{7}$$

$$q(p) = \ln\left(\frac{r_{21}^{p} - s}{r_{32}^{p} - s} \right) \tag{8}$$

$$s = 1 \cdot \operatorname{sgn}\left(\frac{\varepsilon_{32}}{\varepsilon_{21}} \right) \tag{9}$$

where

$$\varepsilon_{21} = \varphi_2 - \varphi_1, \varepsilon_{32} = \varphi_3 - \varphi_2 \tag{10}$$

$q(p) = 0$ when $r_{21} = r_{32}$ and sgn is the signal function. If $\varepsilon_{21}/\varepsilon_{32} < 0$, then sgn = −1. If $\varepsilon_{21}/\varepsilon_{32} = 0$, then sgn = 0. If $\varepsilon_{21}/\varepsilon_{32} > 0$, then sgn = 1.

$$e_a^{21} = \left| \frac{\phi_1 - \phi_2}{\phi_1} \right| \tag{11}$$

$$\phi_{\text{ext}}^{21} = \left| \frac{\left(r_{21}^{p} \phi_1 - \phi_2 \right)}{\left(r_{21}^{p} - 1 \right)} \right|, \phi_{\text{ext}}^{32} = \left| \frac{\left(r_{21}^{p} \phi_2 - \phi_3 \right)}{\left(r_{32}^{p} - 1 \right)} \right| \tag{12}$$

$$e_{\text{ext}}^{21} = \left| \frac{\phi_{\text{ext}}^{12} - \phi_1}{\phi_{\text{ext}}^{12}} \right|, e_{\text{ext}}^{32} = \left| \frac{\phi_{\text{ext}}^{23} - \phi_2}{\phi_{\text{ext}}^{23}} \right| \tag{13}$$

The grid convergence index is expressed as follows:

$$\text{GCI}_{\text{fine}}^{21} = \frac{1.25 e_a^{21}}{r_{21}^{p} - 1}, \text{GCI}_{\text{fine}}^{32} = \frac{1.25 e_a^{32}}{r_{32}^{p} - 1} \tag{14}$$

4.2 Time dependency

In implicit unsteady simulations, the time step selection is typically influenced by the flow characteristics rather than the Courant number. According to the guidelines outlined in ITTC (2021), the time step size (Δt) in calm water can be determined using the formula $\Delta t = 0.005 - 0.01\ L/V$, where L is the distance between the perpendiculars of the ship and V is the velocity of the ship. However, the investigation into time step convergence, aimed at determining the most appropriate time step resolution, revealed the necessity of using a smaller time step ($\Delta t = 0.003\ 5\ L/V$) for this specific study Tezdogan (2016). The value derived from the equation is 0.016 6. The time step was systematically adjusted and investigated at 0.005, 0.01, and 0.02 intervals while maintaining a Fr of 0.105 and a depth of 1.7T.

Table 7 presents the results of the time step convergence analysis at a depth of 1.7T. This study determined the optimal time interval that yields the most accurate resistance prediction while minimizing deviations from predictions made using different time intervals and reducing computation time. This study assessed the convergence of different time intervals and determined that a value of 0.01 produced the most favorable outcomes. The chosen time step exhibited good convergence in the residual plot when altered.

Table 7 Time independency study

Time	Time step	Exp. resistance (N)	Numerical simulation (N)	Difference in percentage
T1	0.005	15.230	14.717	3.37
T2	0.010		14.718	3.36
T3	0.020		14.720	3.35

4.3 Turbulence model

Turbulence modeling plays a crucial role in solving the previously presented equations, and the selection of an appropriate turbulence model is essential for resolving the RANS equations. This study evaluated the RNG $k-\varepsilon$ and shear stress transport (SST) $k-\omega$ turbulence models, as shown in Table 8. Notably, the SST $k-\omega$ turbulence model demonstrated a mere 3.31% disparity between experimental and numerical analyses. Consequently, the SST $k-\omega$ turbulence model was chosen to analyze the fluid dynamics surrounding the hull. The current study employs a simulation model that combines the $k-\varepsilon$ and $k-\omega$ turbulence models, enabling an accurate depiction of the flow dynamics in various scenarios and predicting the corresponding physical changes Jones and Clarke (2010).

Table 8 Turbulence model independency study

Turbulence model	Exp. resistance (N)	Resistance (N)	Difference in percentage
SST $k-\omega$	15.230	14.718	3.36
RNG $k-\varepsilon$		15.765	−3.51

4.4 Experimental results and validation

In the experimental setup, two shallow depths (H/T = 2 and 1.7) were considered and contrasted with the total resistance encountered in deep water. Four distinct Froude numbers were tested, with values between 0.06 and 0.12. The relationship between resistance and Fr for different water depths investigated is shown in Figure 10. The findings of this study indicated that the total resistance of the model exhibited nonlinear characteristics. Theoretically, friction and viscous pressure resistance are the main elements influencing resistance to motion at lower speeds.

However, the role of wave resistance becomes increasingly significant as forward speeds increase, eventually becoming the predominant factor. Notably, a nonlinear correlation between the distance between data points and the water depth is detected. The resistance experienced in shallow water was approximately twice as high as in deep water. According to the Bernoulli principle, a decrease in depth reduces the distance between the hull of the ship and the bottom, increasing the velocity beneath the hull. The reduction in dimensions leads to an alteration in the thickness of the boundary layer, thereby increasing resistance.

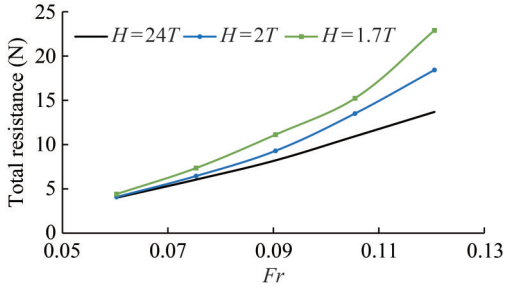

Figure 10 Effect of depth on the experimental total resistance

Figures 11–13 present the comparative analysis of numerical and experimental resistance data for the model hull at $Fr = 0.151$. Three depths were investigated through experimental and numerical analyses: $H = 24T$, $2T$, and $1.7T$ for the Froude numbers 0.05 to 0.121. An assessment was conducted by comparing the total resistance calculated. The comparative analysis revealed a 2% disparity between the resistance values predicted numerically and those measured experimentally in deep water. This discrepancy is further amplified by an additional 3% and 3.2% for other water depths. These figures indicate a strong correlation between the outcomes of the experimental models and the numerical forecasts.

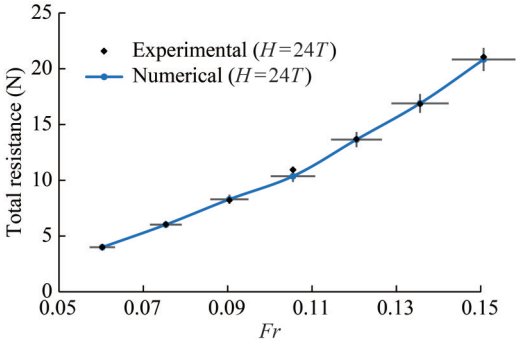

Figure 11 Validation for deep water ($H = 24T$)

5 Results and discussions

5.1 Effect on the boundary layer

The effect of shallow water on the boundary layer was investigated by measuring the thickness of the boundary layer at three distinct locations, namely, the FP, at midship, and near the AP, with $Fr = 0.151$. The depths with $H = 24T$, $2T$, $1.7T$, and $1.5T$ are shown in Figure 14, Figure 15, Figure 16, and Figure 17, respectively.

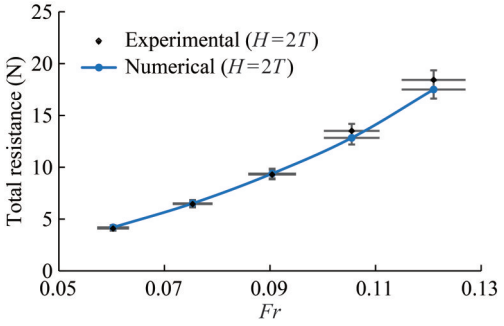

Figure 12 Validation for shallow water ($H = 2T$)

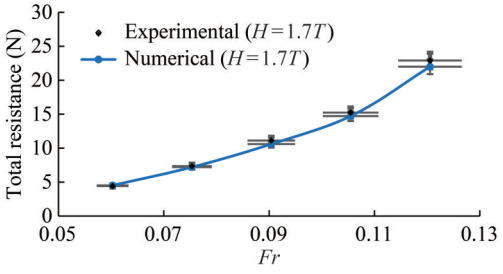

Figure 13 Validation for shallow water ($H = 1.7T$)

Table 9 lists the boundary layer thicknesses at three sections measured at different depths with a constant $Fr = 0.105$. The boundary layer thickens as the flow progresses toward the stern. When a vessel enters shallow waters, the flow velocity increases as the UKC decreases, impeding the formation of the boundary layer beneath the surface of the ship, consequently reducing the boundary layer thickness compared with that under deep water conditions and increasing the velocity gradient inside the boundary layer because of inadequate time for the lateral diffusion of vorticity within the boundary layer (Albernathy, 2000). This increase in velocity gradient escalates shear forces, intensifying the frictional resistance. These factors magnify the influence of viscous forces on ship performance, which is evident from the observed differences in boundary layer thickness between deep and shallow water conditions.

In the stern section (the backside of the skeg), a significant disparity in boundary layer thickness between deep and shallow waters is apparent, where a notable increase in the boundary layer is observed, as shown in Figure 17, which is attributed to the skeg and flow separation becoming more pronounced because of adverse pressure gradients. Consequently, flow separation contributes to an elevation in pressure resistance. The alterations in boundary layer thickness due to the effect of shallow water are illustrated in Figures 14–17. Table 9 provides the magnitude of boundary layer thickness examined under deep and shal-

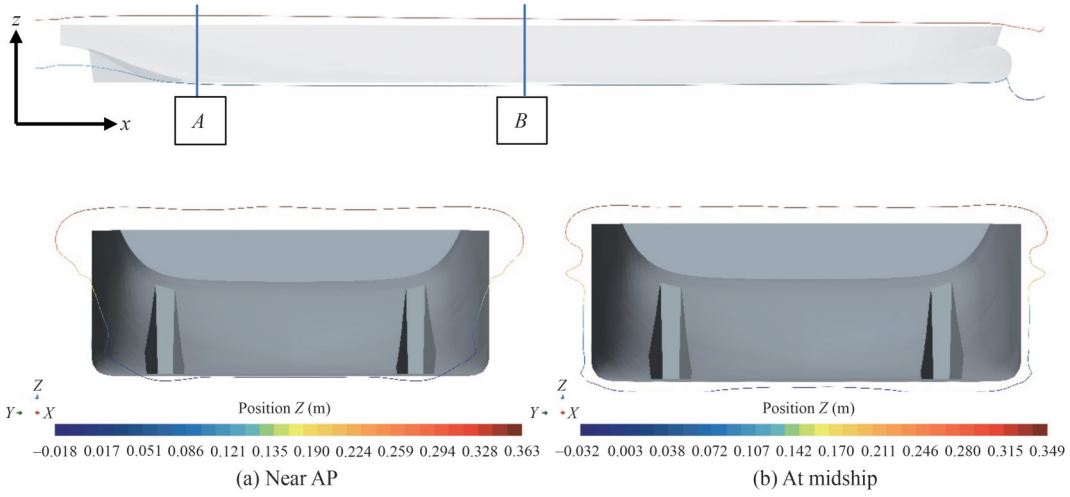

(a) Near AP (b) At midship

Figure 14 Boundary layer thickness for deep water ($H = 24T$)

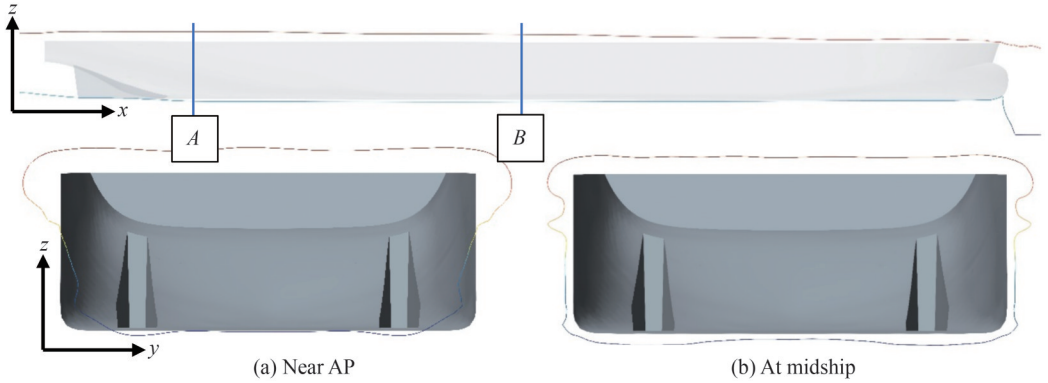

(a) Near AP (b) At midship

Figure 15 Boundary layer thickness for shallow water ($H = 2T$)

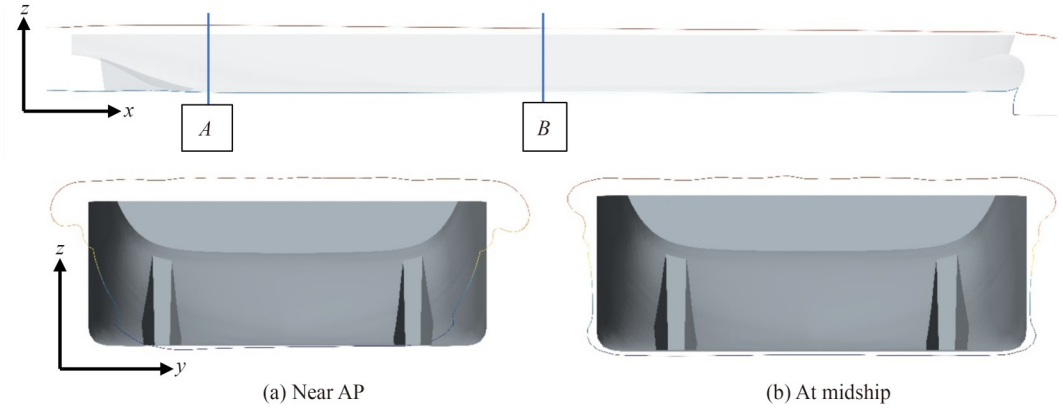

(a) Near AP (b) At midship

Figure 16 Boundary layer thickness for shallow water ($H = 1.7T$)

low water conditions. In deep water at the midship position, the boundary layer thickness is 0.023 9 m. Conversely, in shallow water at the midship position, the boundary layer thicknesses are 0.012 3, 0.010 1, and 0.006 m at their respective depths, as indicated in Table 9. This reduction in boundary layer thickness results in a steeper velocity gradient, increasing shear stress as water depth decreases. Consequently, frictional resistance also increases with the decrease in water depth.

5.2 Effect on the shear stress

The effect of shallow water on shear stress distribution was analyzed by measuring the shear stress in three distinct sections, namely, the bow section, parallel middle body, and stern section. Figure 18 illustrates the shear stress variation along the length of the ship at the bow, midship, and stern sections for different water depths (i.e., deep and shallow waters) at $Fr = 0.151$. Under deep water

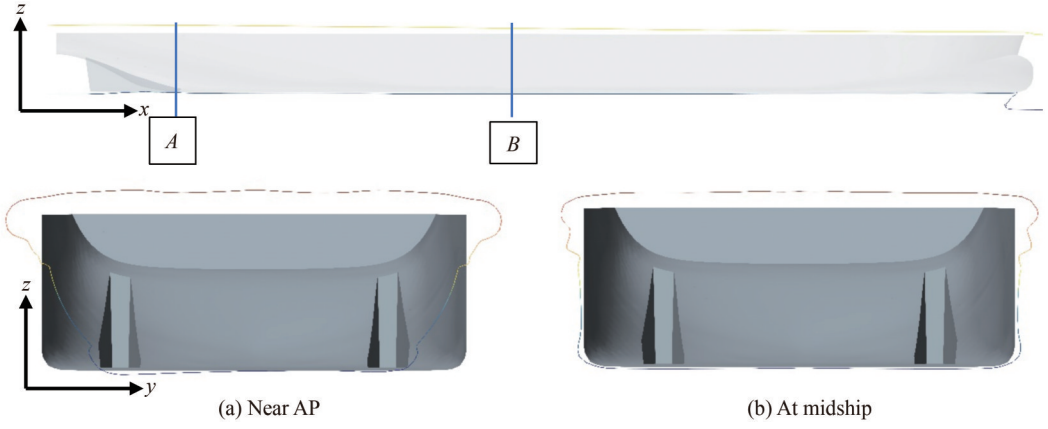

(a) Near AP (b) At midship

Figure 17 Boundary layer thickness for shallow water ($H = 1.5T$)

Table 9 Boundary layer thickness for different depths

Depth	At FP (m)	At midship (m)	Near AP (m)
$H = 24T$	0.000 8	0.023 9	0.001 9
$H = 2T$	0.000 7	0.012 3	0.001 3
$H = 1.7T$	0.000 3	0.010 1	0.001 2
$H = 1.5T$	0.000 1	0.006 0	0.001 3

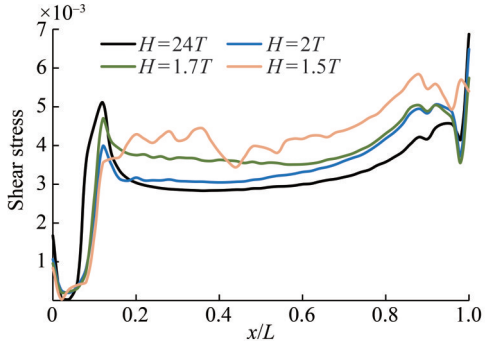

Figure 18 Shear stress at different depths

conditions, the flow in the entrance region shows increased momentum, resulting in elevated levels of shear stress, particularly on the fore shoulder of the ship. The velocities on the upper portion of the bulbous bow exhibit a comparatively low magnitude, leading to reduced shear stress caused by stagnation. A relatively uniform shear stress level is observed along the midship region. Flow along the keel, particularly near the skeg area, has a vertical velocity component, resulting in a modest increase in shear stress. Flow separation near the stern edge leads to a decrease in shear stress. A notable increase in shear stress is observed when transitioning from deep to shallow water depths. Sailing in shallow water is further influenced by the presence of the water bottom, causing additional changes in shear stress. As the flow beneath the hull accelerates, the velocity near the bow shoulder increases, resulting in higher shear stress.

With the decrease in depth, the velocity variation spreads toward the midship. Notably, the stress distribution in the bow and stern sections exhibits significant variation compared with that in the midship region. At a depth of $1.5T$, the fluctuation in shear stress is considerably higher than that of other depths. The shear stress is consistently lower in the midship area than in the bow and stern regions for all depths, including deep and shallow water conditions. This occurrence can be explained by the significant disparity in velocity between the regions near the bow and the stern, as opposed to the relatively stable conditions in the midship region. When we examined the entire submerged portion of the hull, we observed a significant increase in the average shear stress as the water depth decreased. Notably, the impact of shallow water on the boundary layer increases shear stress and frictional resistance.

5.3 Effect on the frictional resistance

Figure 19 illustrates the frictional resistance coefficient at four different depths (i.e., $H = 24T$, $2T$, $1.7T$, and $1.5T$) with Fr ranging from 0.06 to 0.151. As the velocity increases, the frictional resistance coefficient correspondingly decreases. At low Fr, the water depth significantly affects the frictional resistance.

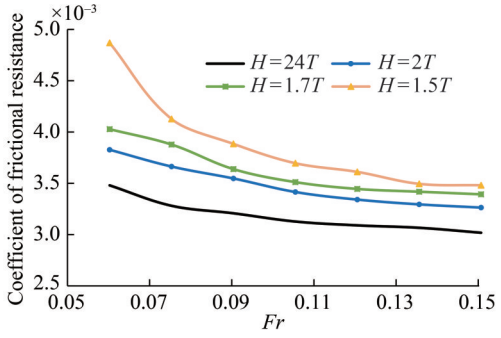

Figure 19 Effect of depth on the frictional resistance coefficient

The frictional resistance coefficients for a case with $Fr = 0.06$ at different depths were examined. The frictional resistance coefficient increases by approximately 45% for $H = 1.5T$ compared with that under deep water conditions. The percentage increase in frictional resistance coefficient

for higher *Fr* values is approximately 11%. The impact of the shallow water effect is high at lower speeds. Sinkage increases in shallow water because of the accelerated flow beneath the hull. Consequently, the wetted surface area increases, and the combined effect of increased wetted surface area and shear stress further contributes to increased frictional resistance.

5.4 Effect on the velocity and pressure

Figures 20, 22, and 26 illustrate the velocity distribution at the bow and stern sections of a mini-bulk carrier, considering all water depths at $Fr = 0.15$. As the vessel moves into shallower waters, the reduced water depth results in a narrower gap between the hull surface and the seafloor, which, according to the Bernoulli principle, leads to an increase in water velocity and a corresponding decrease in water pressure beneath the hull. The aforementioned figures indicate that the velocity near the front and rear ends is higher in shallow waters than in deep waters. Notably, velocity fluctuations in the bow shoulder region are more significant than those in the stern area. In addition, velocity fluctuations are less pronounced at the midship section than in the stern and bow sections under shallow water conditions. However, velocity exhibits more significant variation as water depth decreases, leading to a decrease in water pressure beneath the hull, as illustrated in the aforementioned figures.

Figures 21, 23, 25, and 27 show the variations in pressure distribution along the surface of the hull at various water depths. Notably, the pressure below the hull is significantly less in the midship section than in the bow section. As the water depth decreases, the high-pressure area ahead of the bow and the pressure difference between the bow and stern increases, causing an uneven pressure distribution along the hull (Su et al., 2023). In addition, this extensive low-pressure region shifts outward, trailing behind the ship and toward the bow (upstream). Hence, the flow velocity between the hull surface and the seabed significantly increases, causing substantial alterations in pressure. Because of the decreased pressure, the buoyant force acting on the hull decreases. To counter this reduced pressure, the vessel sinks deeper in shallow waters than in deep waters, resulting in increased draft or sinkage.

Figure 20 Velocity distribution in deep water ($H = 24T$)

Figure 21 Pressure distribution in deep water ($H = 24T$)

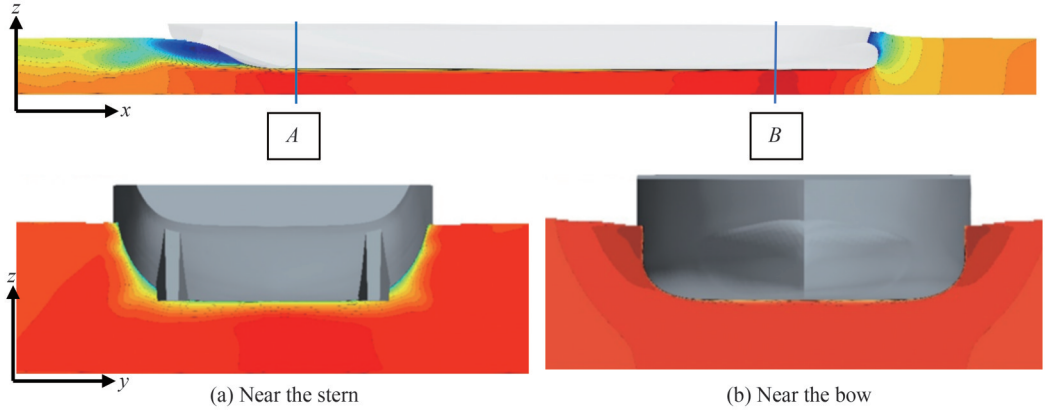

Figure 22 Velocity distribution in shallow water ($H = 2T$)

Figure 23 Pressure distribution on the hull surface in shallow water ($H = 2T$)

Figure 24 Velocity distribution in shallow water ($H = 1.7T$)

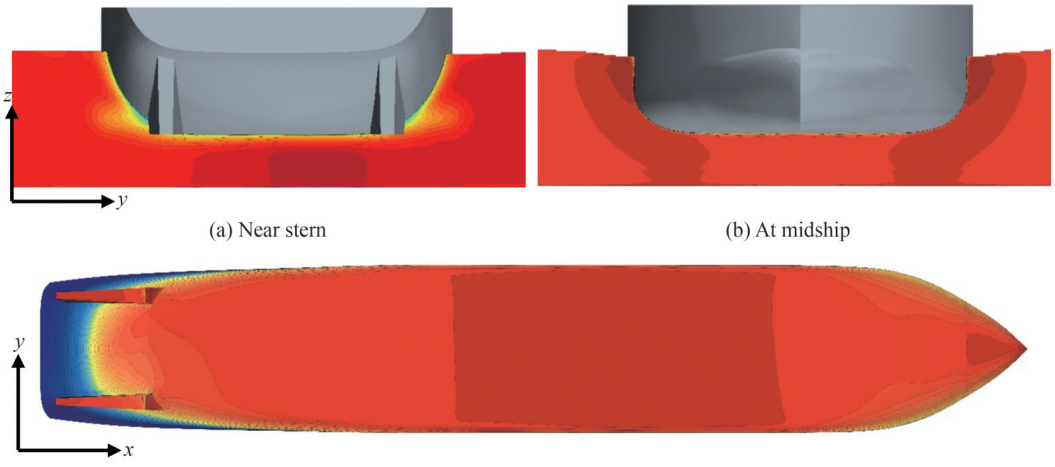

Figure 25 Pressure distribution in shallow water ($H = 1.7T$)

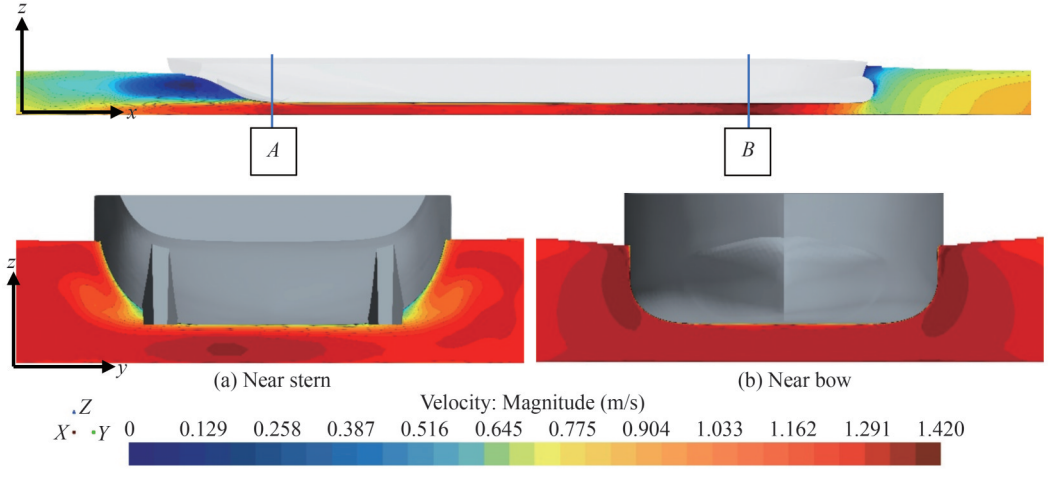

Figure 26 Velocity distribution in shallow water ($H = 1.5T$)

Figure 26 depicts the escalation in the velocity distribution at the depth $H = 1.5T$. The velocity magnitude increases up to 1.4 m/s in the bow and stern regions, which is higher than for deep and shallow waters. However, with the decrease in water depth, the increase in velocity becomes more pronounced. On average, the velocity at the stern section increases by 20% and that at the bow section increases by approximately 15%, causing a reduction in pressure in areas with increased velocity.

5.5 Effect on the turbulence

The impact of turbulence on ship resistance is examined

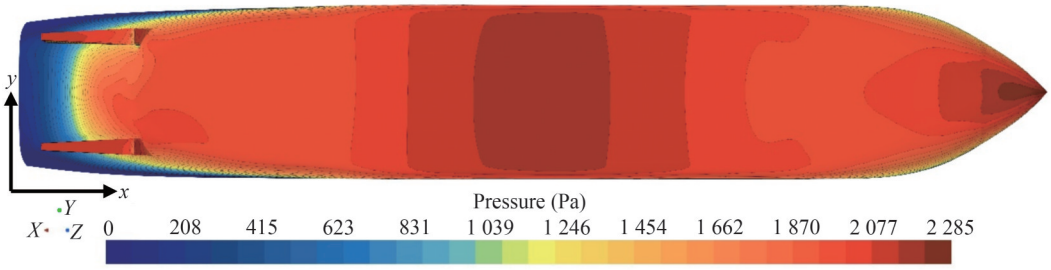

Figure 27 Pressure distribution on the hull surface in shallow water ($H = 1.5T$)

through TKE and turbulent viscosity. Figure 28 compares the TKE at the stern of the model under deep and shallow water conditions at $Fr = 0.151$. The flow pattern conforms to the contours of the vessel from the bow to the stern. Near the stern, the flow experiences an abrupt change because of the curvature of the hull form, resulting in pressure fluctuations and detachment from the hull, leading to recirculation and turbulence. This gap may be more pronounced under shallow water conditions because of the proximity of the seabed. The confined space in shallow waters limits the lateral spread of the wake, intensifying wake-related effects, such as turbulence (Shevchuk and Kornev, 2017). This turbulent wake enhances the resistance by generating localized zones in the stern region. Figure 28(a) illustrates the TKE under deep water conditions. Figures 28(b), 28(c), and 28(d) depict the TKE under shallow water conditions with corresponding depths of $2T$, $1.7T$, and $1.5T$, respectively. Notably, the stern region exhibits increased turbulence and energy loss. This finding shows that the TKE in the stern region generally increases under shallow water conditions, indicating substantial energy loss from the hull. The strength of recirculation increases as water depth decreases, leading to an intensified wake zone.

Figure 29 depicts the turbulent viscosity near the hull surface under deep and shallow water conditions at $Fr = 0.151$. As a vessel transitions from deep to shallow waters, the confined space alters the flow behavior, leading to increased turbulence within the boundary layer. Under deep water conditions, the local Reynolds number in the entrance region is lower, resulting in less turbulence and lower turbulent viscosity. However, as the length of the ship increases, the local Reynolds number increases, leading to increased turbulence and turbulent viscosity. Flow separation occurs near the stern section, reducing turbulence. By contrast, turbulent viscosity increases far from the stern section because of the adverse pressure gradient. As depth decreases, turbulent viscosity gradually increases, especially at the midship region. For a depth of $1.5T$, turbulent viscosity increases compared with other depths because of the reduced boundary layer effect. Near the stern section, the increase in turbulent viscosity is similar for all depths but higher than that under deep water conditions. When water particles near the hull of a ship exhibit turbulent motion, their interactions with the hull surface intensify; this increased interaction leads to higher energy dissipation between the moving water and the hull, resulting in elevated Reynolds stress. As a consequence, viscous resistance increases.

Eddy and turbulent viscosity refer to the viscosity associated with turbulent flows. As turbulence intensifies within the boundary layer, the Reynolds stress increases. This increase in Reynolds stress can be detected by measuring turbulent viscosity within the boundary layer. The illustration visually represents the increase in turbulent viscosity near the surface of the vessel as the water depth decreases.

5.6 Effect on the waves

The depth Froude number, Fr_h, is crucial in analyzing shallow water dynamics (Terziev et al., 2018). This parameter categorizes the speed of a vessel into three distinct categories, namely subcritical ($Fr_h < 1$), critical ($Fr_h = 1$), and supercritical ($Fr_h > 1$). Different ship speeds correspond to wave patterns, which undergo notable changes as a vessel approaches its critical speed. In this study, the speeds consistently fell below the value of the depth Froude number of $Fr_h = 0.612$. The wave patterns in this range closely resemble those under deep water conditions, as depicted in Figure 30. Figures 30(a), 30(b), 30(c), and 30(d) show the free surface elevation for $H/T = 24$, 2, 1.75, and 1.5, respectively. The value of $x/L = 1$ refers to the bow; the positive value of x/L indicates the direction of moving forward (toward the inlet), and the negative value of x/L indicates the direction of moving toward aft (outlet boundary). Figure 31 depicts the bow wave elevation under different depth conditions. The wave height near the bow increases as the water depth decreases, resulting in enhanced energy transfer between the hull and the wave, which causes increased wave resistance.

Regarding the stern, Figure 32 shows that the wave height increases under deep ($H/T = 24$) and shallow (H/T up to 2) water conditions. For H/T up to 1.7, the stern wave first decreases and then increases with a further decrease in depth ($H/T < 1.5$). These waves usually pass by the ship with little resistance in deep water. However, these waves behave differently in shallow waters because of their close-

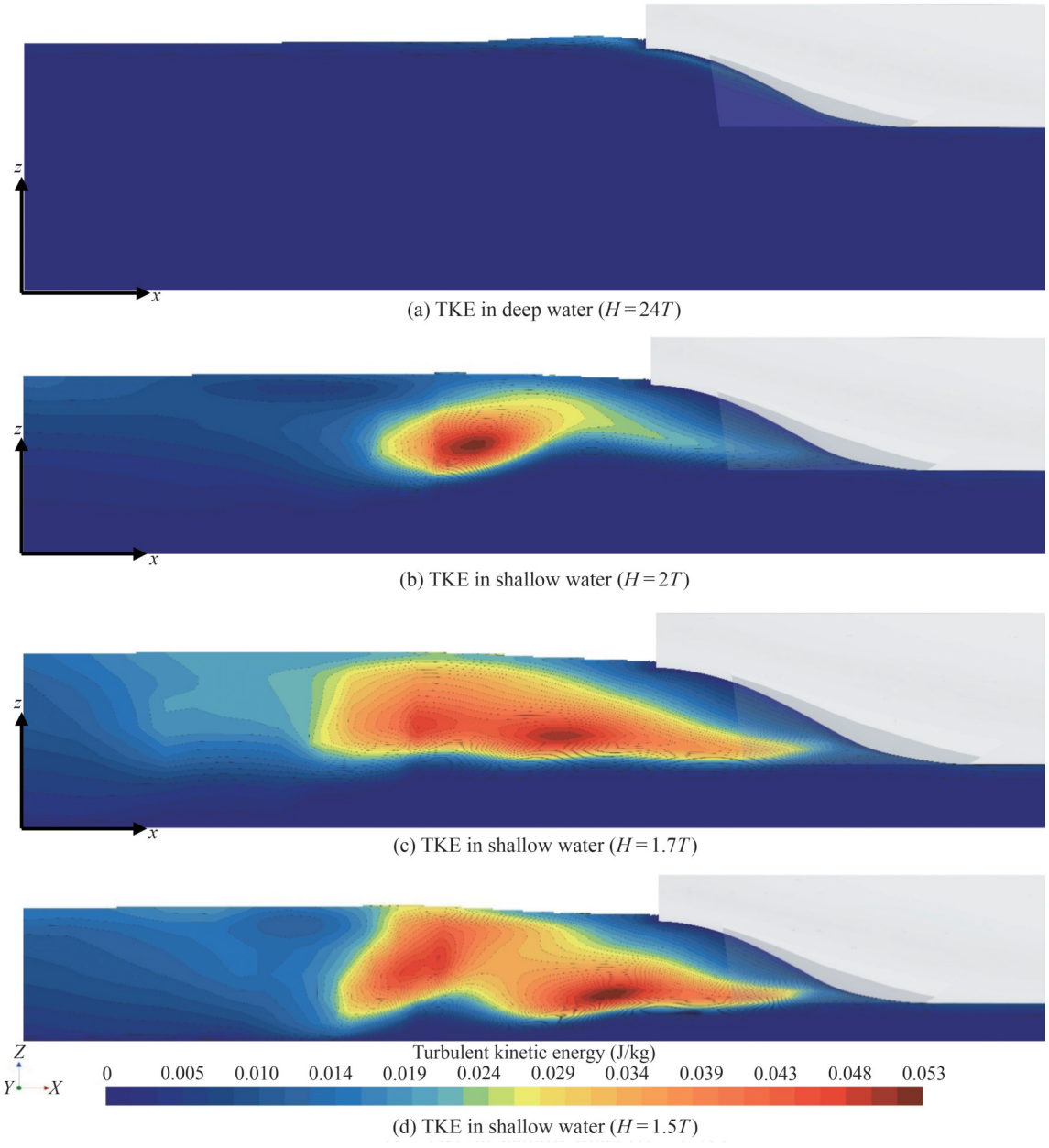

Figure 28 Turbulent kinetic energy (TKE) at different depths

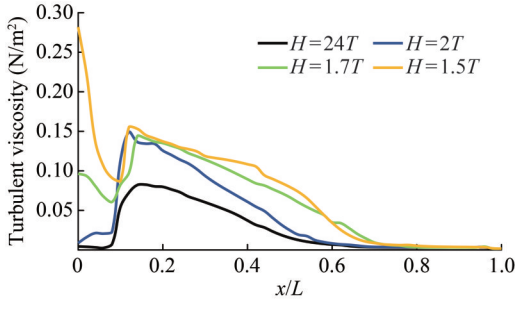

Figure 29 Effect of depth on the turbulent viscosity

ness and interaction with the seabed. In addition to the waves created by the ship, this reflection may cause other waves to be formed. When these waves are combined, interference patterns that include both constructive and destructive interference zones are generated. Wave amplitudes build up in constructive interference areas, producing more prolonged and intense waves, which can be inferred from Figure 30(d).

Figure 31 illustrates the increase in the bow wave height as the water depth decreases in shallower waters. A reduced UKC limits the flow space of the water, causing more kinetic energy to transform into the potential energy of the wave, leading to taller bow waves. The limited depth restricts wave propagation, causing waves to become steeper and taller; this increase in wave height results in elevated wave

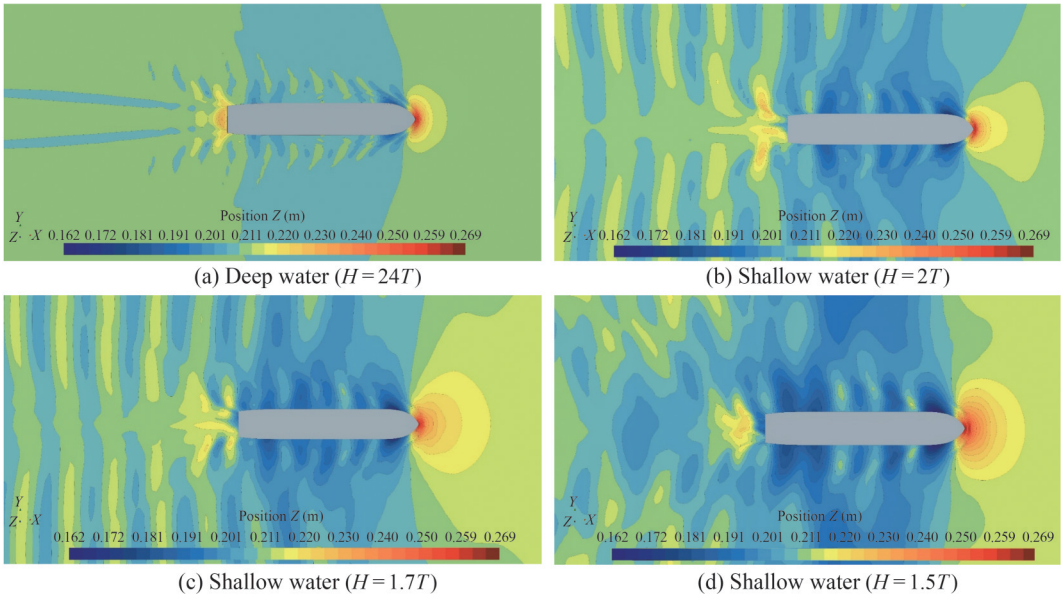

Figure 30 Wave patterns at different water depths

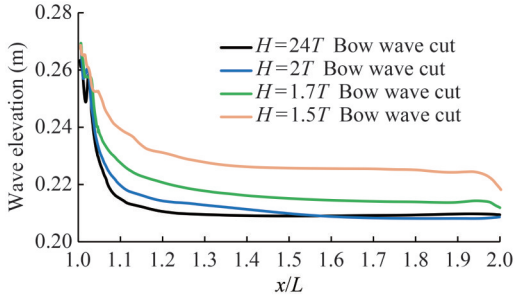

Figure 31 Bow wave elevation at different depths

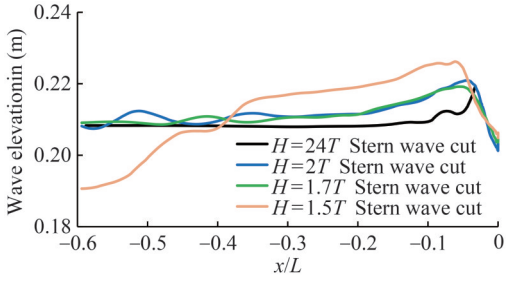

Figure 32 Stern wave elevation at different depths

resistance. Although the wave height under shallow water conditions increases with a decrease in water depth, the Kelvin wave pattern formed by the ship under shallow water conditions resembles that under deep water conditions, as shown in Figure 30.

5.7 Effect on the total resistance

Figure 33 depicts the effect of water depth on the percentage increase in total resistance with *Fr* ranging between 0.06 and 0.151. Frictional resistance dominates at lower speeds, whereas wave resistance becomes more significant at higher speeds. For instance, at lower speeds (*Fr* = 0.06), the relative increase in total resistance compared with deep water conditions (baseline value) is 5%. At *H*/*T* = 1.7, this increase in total resistance reaches 13%, and at *H*/*T* = 1.5, it becomes even more pronounced. This trend is consistent across all speeds and water depths. At lower Froude numbers, frictional and viscous resistance are the primary factors influencing resistance. However, as the depth decreases, the pressure within the vortex core decreases further at higher Froude numbers in shallow water. This phenomenon can lead to a greater pressure disparity between the bow and the stern, resulting in a more substantial form factor. The shallow water form factor varies as *H*/*T* is reduced, and for higher Froude numbers, wave resistance increases because of heightened wave height and accelerated flow. The increase in total resistance is attributed to the shallow water effect, where both viscous and pressure resistance components are influenced by increased wetted surface area and enhanced wave-making capability, respectively.

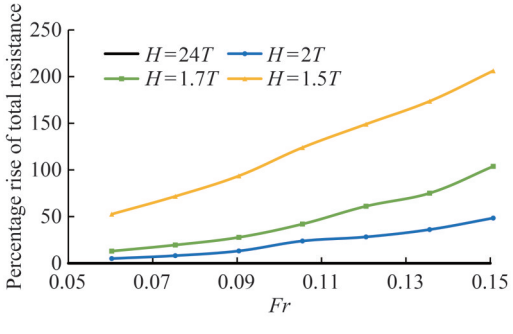

Figure 33 Percentage of increase of the total resistance compared with deep water

6 Conclusions

The present study comprehensively analyses the hydrodynamic characteristics of a mini-bulk carrier vessel in shallow water. The investigation involves conducting experimental and numerical analyses to evaluate the resistance of the vessel in various scenarios, including deep and shallow water conditions. This study is limited to the effect of shallow water on resistance and flow dynamics. However, this study provides significant insights into optimal approaches for investigating the impact of shallow water on resistance. Based on the findings and subsequent examination, we derive the following conclusions:

1) The resistance values obtained using numerical methods were validated by comparing them with the experimental results, demonstrating the efficacy of the numerical approach and illustrating the capability of the RANS-based technology in predicting the resistance of mini-bulk carrier vessels in both deep and shallow waters. Despite their efficiency, RANS models are based on turbulence structure assumptions, which could lead to errors in complex flows with separation and recirculation and difficulty in accurately predicting complex flow phenomena. When conducting numerical modeling in shallow water, special care must be taken to account for the complex interaction between the hull and the bottom.

2) A mini-bulk carrier ship was investigated to evaluate the overall resistance at various velocities in shallow water depths. The frictional drag increases progressively as the water depth decreases from deep to shallow. However, residual resistance substantially increases when compared with frictional resistance.

3) An investigation was conducted to examine the primary factors that influence resistance caused by shallow water. The primary focus of this study was to examine the impact of five key factors, namely, boundary layer thickness, shear stress, velocity and pressure, turbulence, and waves, on resistance.

4) The decreasing depth influences the flow acceleration underneath the hull because of its proximity to the floor. Consequently, the thickness of the layer diminishes, leading to an augmented velocity gradient within the boundary layer, which, in turn, results in the elevation of shear stress and resistance.

5) When a vessel increases its speed in shallow water, the distance between the hull of the ship and the seabed decreases. This phenomenon leads to a decrease in water pressure beneath the hull and causes an elevation in sinkage, leading to a more substantial water displacement. The observed phenomenon of displacement results in the corresponding elevation in resistance.

6) Shallow water conditions frequently increase turbulence, and a decrease in the boundary layer leads to intensified turbulence. These changes inside the boundary layer have the most significant impact on Reynolds stress. Greater friction and viscous resistance can result from more effective interactions between the hull, water, and seafloor.

7) Pressure gradients along the surface of the hull might fluctuate. These pressure gradients can cause the flow to detach and reconnect, resulting in turbulent eddies and vortices that increase the overall turbulence beneath the ship and, therefore, the resistance.

8) As a ship sails across the water, it generates waves at the bow and stern. These waves travel largely unobstructed away from the ship in deeper waters. However, the proximity of the surface in shallow waters influences the behavior of these waves. As a consequence, the wave resistance increases.

9) Wave amplitudes in shallow waters can become massive because of constructive interference, resulting in nonlinear effects. These nonlinear effects can cause waves to break more easily, which, in turn, causes wave-breaking resistance to increase.

10) Compared with deep water resistance, the percentage of resistance increase is twice for the $1.7T$ depth. However, in contrast to the $1.7T$ depth, the proportional increase for the $1.5T$ depth is significant.

Nomenclature

ALS	Air lubrication system
CFD	Computational fluid dynamics
EEDI	Energy Efficiency Design Index
EEXI	Energy Efficiency Existing Ship Index
ITTC	International Towing Tank Conference
MEPC	Marine Environment Protection Committee
UKC	Under keel clearance
m	Blockage factor
δ	Boundary layer thickness
ΔV	Change in velocity
C_F	Coefficient of frictional resistance
Fr_h	Depth Froude number
T	Draft of the ship
μ	Dynamic viscosity
R_F	Frictional resistance of ship in N or KN
Fr	Froude number
H	Height of the channel or water depth
v	Kinematic viscosity
τ	Shear stress in Pa
S	Ship wetted surface area in m
Y	Sidewall distance in m
U or V	Speed of the ship or speed of the flow in m/s
R_T	Total resistance in N or KN
$\mathrm{d}u/\mathrm{d}y$	Velocity gradient
R_v	Viscous resistance in N or KN

Funding Supported by the Ministry of Shipping, India (Grant No. OEC/18-19/157/MOSH/RVIJ).

Acknowledgement The authors express their gratitude to Gouthama Chary Soma and Hemanth Kumar for their manuscript review. Additionally, the authors extend their appreciation to Gouthama Chary Soma, Prabkirat Singh, Gokulakrishnan, and Guggila Mukesh for their valuable assistance during the experimental study. The author would acknowledge AICTE and Sri Shakthi Institute of Engineering and Technology, Coimbatore, for providing necessary support. The authors also acknowledge the computational support extended by the High-Performance Computing Environment (HPCE) of IIT Madras.

Competing interest The authors have no competing interests to declare that are relevant to the content of this article.

References

Albernathy FH (2000) Fundamentals of boundary-layer theory. Boundary-Layer Theory. https://doi.org/10.1007/978-3-642-85829-1_2

Best practices for ship resistance test simulations in shallow water [WWW Document] (2019) Star CCM+. URL https://support.sw.siemens.com/knowledge-base/KB000040297_EN_US

Celik IB, Ghia U, Roache PJ, Freitas CJ, Coleman H, Raad PE (2008) Procedure for estimation and reporting of uncertainty due to discretization in CFD applications. J. Fluids Eng. Trans. ASME 130: 0780011-0780014. https://doi.org/10.1115/1.2960953

Chen C, Delefortrie G, Lataire E (2021) Effects of water depth and speed on ship motion control from medium deep to very shallow water. Ocean Eng. 231: 109102. https://doi.org/10.1016/j.oceaneng.2021.109102

Elsherbiny K, Terziev M, Tezdogan T, Incecik A, Kotb M (2020) Numerical and experimental study on hydrodynamic performance of ships advancing through different canals. Ocean Eng. 195: 106696. https://doi.org/10.1016/j.oceaneng.2019.106696

Gorbachev Y, Amromin E (2012) Ship drag reduction by hull ventilation from laval to near future: challenges and successes. Maritime and Aeronautical Technical Association

Hemanth Kumar Y, Vijayakumar R (2020a) Effect of flap angle on transom stern flow of a high speed displacement surface combatant. Ocean Syst. Eng. 10: 1-23. https://doi.org/10.12989/ose.2020.10.1.001

Hemanth Kumar Y, Vijayakumar R (2020b) Development of an energy efficient stern flap for improved EEDI of a typical high-speed displacement vessel. Def. Sci. J. 70: 95-102. https://doi.org/10.14429/dsj.70.14669

ITTC (2021) ITTC-Recommended Procedures and Guidelines Practical Guidelines for Ship Resistance CFD ITTC Quality System Manual Recommended Procedures and Guidelines Guideline Practical Guidelines for Ship Resistance CFD

ITTC (2011) Practical Guidelines for Ship CFD Applications, ITTC–Recommended Procedures and Guidelines ITTC

Jebin Samuvel T, Gokulakrishnan KA, Vijayakumar R (2022) Numerical estimation of frictional drag on flat plate in shallow water with & without BDR. OCEANS 2022-Chennai. IEEE 1-7. https://doi.org/10.1109/OCEANSChennai45887.2022.9775316

Jiang T (2001) A new method for resistance and propulsion prediction of ship performance in shallow water. Eighth International Symposium on Practical Design of Ships and Other Floating Structures, Shanghai, China, 509-515. https://doi.org/https://doi.org/10.1016/B978-008043950-1/50064-8

Ji SC, Ouahsine A, Smaoui H, Sergent P (2012) 3-D numerical simulation of convoy-generated waves in a restricted waterway. J. Hydrodyn. 24: 420-429. https://doi.org/10.1016/S1001-6058(11)60263-1

Jones DA, Clarke DB (2010) Fluent code simulation of flow around a naval hull: the DTMB 5415, maritime platforms division-DSTO. Defence Science and Technology Organisation

Kumar M, Anantha Subramanian V (2007) A numerical and experimental study on tank wall influences in drag estimation. Ocean Eng. 34: 192-205. https://doi.org/10.1016/j.oceaneng.2005.10.025

Lackenby H (1964) The effect of shallow water on ship speed. Nav. Eng. J. 76: 21-26. https://doi.org/10.1111/j.1559-3584.1964.tb04413.x

Lataire E, Vantorre M, Delefortrie G (2012) A prediction method for squat in restricted and unrestricted rectangular fairways. Ocean Eng. 55: 71-80. https://doi.org/10.1016/j.oceaneng.2012.07.009

Li M, Yuan ZM, Tao L (2023) Wash waves generated by ship moving across a depth change. Ocean Eng. 275: 114073. https://doi.org/10.1016/j.oceaneng.2023.114073

Mucha P (2017) On simulation-based ship maneuvering prediction in deep and shallow water. University of Duisburg-Essen, 1-177

Mucha P, Moctar O. el, Dettmann T, Tenzer M (2018) An experimental study on the effect of confined water on resistance and propulsion of an inland waterway ship. Ocean Eng. 167: 11-22. https://doi.org/10.1016/j.oceaneng.2018.08.009

Muzaferija S, Peric M (2017) Computation of free-surface ows using interface- tracking and interface-capturing methods. In: numerical modeling of radiative heat transfer in multiphase flows with free surface

Raven HC (2012) A computational study of shallow-water effects on ship viscous resistance. Proceedings of the 29th Symposium on Naval Hydrodynamics Gothenburg, 26-31

Raven HC (2018) A method to correct shallow-water model tests for tank wall effects. J. Mar. Sci. Technol. 24: 437-453. https://doi.org/10.1007/s00773-018-0563-1

Raven HC (2019) Shallow-water effects in ship model testing and at full scale. Ocean Eng. 189: 106343. https://doi.org/10.1016/j.oceaneng.2019.106343

Richardson (1910) On the approximate arithmetical solution by finite differences of physical problems involving differential equations, with an application to the stresses in a masonry dam. Proceedings of the Royal Society of London. Series A, Containing Papers of a Mathematical and Physical Character, 335-336. https://doi.org/10.1098/rspa.1910.0020

Rotteveel E, Hekkenberg RG (2015) The influence of shallow water and hull form variations on inland ship resistance. Proceedings of the 12th International Marine Design Conference, 11-14

Schlichting O (1934) Ship resistance in water of limited depth-resistance of sea-going vessels in shallow water. U.S. Experimental model basin, Navy yard

Shevchuk I, Kornev N (2017) Study of unsteady hydrodynamic effects in the stern area of river cruisers in shallow water. Sh. Technol. Res. 440-448. https://doi.org/10.1080/09377255.2017.1349599

Sindagi S, Saxena BK (2016) Frictional drag reduction: an EFD and CFD-based review of mechanisms. RINA-MARHY

Sindagi S, Vijayakumar R (2020) Succinct review of MBDR/BDR technique in reducing ship's drag. Ships Offshore Struct. 16: 1-12. https://doi.org/10.1080/17445302.2020.1790296

Sindagi S, Vijayakumar R, Saxena BK (2021) Experimental

investigation on ship's model in carrying out energy economics of BDR/ALS methodology. Ships Offshore Struct. 17: 1-10. https://doi.org/10.1080/17445302.2021.1926147

Sindagi S, Vijayakumar R, Saxena BK (2020a) Parametric CFD investigation of ALS technique on reduction in drag of bulk carrier. Ships Offshore Struct. 15: 417-430. https://doi.org/10.1080/17445302.2019.1661617

Sindagi S, Vijayakumar R, Saxena BK (2020b) Experimental parametric investigation to reduce drag of a scaled model of bulk carrier using BDR/ALS technique. J. Sh. Res. 0: 1-9. https://doi.org/10.5957/josr.02190009

Soma GC, Vijayakumar R (2023a) Numerical investigation on the effect of hull vane for a high-speed displacement vessel. Ships Offshore Struct. 19: 1-14. https://doi.org/10.1080/17445302.2023.2239541

Soma GC, Vijayakumar R (2023b) Hydrodynamic performance of high-speed displacement vessel with hull vane. Ocean Eng. 285: 115362. https://doi.org/10.1016/j.oceaneng.2023.115362

Song S, Terziev M, Tezdogan T, Demirel YK, De Marco Muscat-Fenech C, Incecik A (2023) Investigating roughness effects on ship resistance in shallow waters. Ocean Eng. 270: 113643. https://doi.org/10.1016/j.oceaneng.2023.113643

Su S, Wu Y, Xiong Y, Guo F, Liu H, Cheng Q (2023) Experiment and numerical simulation study on resistance performance of the shallow-water seismic survey vessel. Ocean Eng. 279: 113889. https://doi.org/10.1016/j.oceaneng.2023.113889

Tabaczek T (2008) Computation of flow around inland waterway vessel in shallow water: Archives of Civil and Mechanical Engineering, Committee of Civil and Mechanical Engineering, 97-105. https://doi.org/10.1016/s1644-9665(12)60269-6

Tang X, Tong S, Huang G, Xu G (2020) Numerical investigation of the maneuverability of ships advancing in the non-uniform flow and shallow water areas. Ocean Eng. 195: 106679. https://doi.org/10.1016/j.oceaneng.2019.106679

Terziev M, Tezdogan T, Incecik A (2021) A numerical assessment of the scale effects of a ship advancing through restricted waters. Ocean Eng. 229: 108972. https://doi.org/10.1016/j.oceaneng.2021.108972

Terziev M, Tezdogan T, Oguz E, Gourlay T (2018) Numerical investigation of the behaviour and performance of ships advancing through restricted shallow waters. J. Fluids Struct. 76: 185-215. https://doi.org/10.1016/j.jfluidstructs.2017.10.003

Tezdogan T (2016) A numerical investigation of the squat and resistance of ships advancing through a canal using CFD. J. Mar. Sci. Technol. 21: 86-101. https://doi.org/10.1007/s00773-015-0334-1

Tezdogan T, Incecik A, Turan O (2016) Full-scale unsteady RANS simulations of vertical ship motions in shallow water. Ocean Eng. 123: 131-145. https://doi.org/10.1016/j.oceaneng.2016.06.047

Tripathi S, Vijayakumar R (2024) Numerical and experimental study of stern flaps impact on resistance and propulsion of high–speed displacement ships. Ocean Eng. 292: 116483 https://doi.org/10.1016/j.oceaneng.2023.116483

Tuck EO (1978) Hydrodynamic problems of ships in restricted waters. Annu Rev Fluid Mech. 33-46. https://doi.org/10.1146/annurev.fl.10.010178.000341

Vantorre M, Verzhbitskaya E, Laforce E (2002) Model test of ship-to-ship interaction forces. Sh. Technol. Res. 49: 124-141

Xu HF, Zou ZJ, Wu SW, Liu XY, Zou L (2017) Bank effects on ship–ship hydrodynamic interaction in shallow water based on high-order panel method. Ships Offshore Struct. 12: 843-861. https://doi.org/10.1080/17445302.2016.1275475

Zeng Q, Hekkenberg R, Thill C (2019a) On the viscous resistance of ships sailing in shallow water. Ocean Eng. 190: 106434. https://doi.org/10.1016/j.oceaneng.2019.106434

Zeng Q, Hekkenberg R, Thill C, Rotteveel E (2017) A numerical and experimental study of resistance, trim and sinkage of an inland ship model in extremely shallow water. Int. Conf. Comput. Appl. Shipbuild. 1-28. https://doi.org/10.2514/6.1994-2384

Zeng Q, Thill C, Hekkenberg R (2018) A benchmark test of ship resistance in extremely shallow water. Prog. Marit. Technol. Eng. Proc. 4th Int. Conf. Marit. Technol. Eng. MARTECH. 221-232. https://doi.org/10.1201/9780429505294-26

Zeng Q, Thill C, Hekkenberg R, Rotteveel E (2019b) A modification of the ITTC57 correlation line for shallow water. J. Mar. Sci. Technol. 24: 642-657. https://doi.org/10.1007/s00773-018-0578-7